

Nonlinearity Compensation for Coherent Optical Satellite Communications

Stella Civelli, *Member, IEEE*, Luca Potì *Senior Member, IEEE*, Enrico Forestieri, *Life Member, IEEE*, and Marco Secondini, *Senior Member, IEEE*

Abstract—Optical satellite uplinks rely on high-power optical amplifiers (HPOAs) to overcome free-space attenuation and enable long-distance transmission. However, at high power levels, fiber Kerr nonlinearity becomes significant and degrades system performance. In this work, we develop a realistic model for optical uplinks that accounts for nonlinear effects and analyze their impact, highlighting key differences from conventional long-haul fiber systems. We then introduce low-complexity digital signal processing techniques for nonlinearity compensation, based on constellation shaping via a look-up table (LUT) and a simple nonlinear phase rotation applied at the transmitter and/or receiver. The LUT also enables adaptive rate tuning according to channel conditions, enhancing robustness against link variations. Simulation results show that the proposed techniques increase the maximum acceptable link loss by up to 6 dB with negligible complexity. Finally, we show that, at the system level, propagation in the HPOA can be modeled as a simple nonlinear phase rotation, equivalent to propagation in a zero-dispersion noiseless fiber link, and fully characterized by a single parameter—the characteristic nonlinear power.

Index Terms—Optical satellite communication, nonlinear optical channel, high power optical amplifiers.

I. INTRODUCTION

RECENTLY, optical satellite communication has emerged as an effective technology to complement—and potentially replace—conventional radio-frequency (RF) satellite links [1]–[4]. Ground-to-satellite optical links, however, suffer from severe impairments caused by time-varying atmospheric conditions and by the relative motion between the satellite and the Earth (i.e., varying pointing angle), both leading to significant attenuation and performance degradation. To ensure sufficient received power at the satellite, thereby improving throughput and maintaining resilience under adverse conditions, the launch power should be as high as possible.

While free-space optical communications (FSOC) provide several advantages for satellite networks, the ground-to-satellite uplink remains a critical challenge [5]. Its performance is significantly affected by atmospheric phenomena such as scattering [1], molecular absorption [3], and turbulence [6]. Connectivity losses caused by cloud coverage can be mitigated through the use of optical ground station diversity [7], and

adaptive optics techniques are commonly employed to reduce beam distortions induced by atmospheric turbulence [8]. However, even with these mitigation strategies, a fundamental asymmetry persists between the uplink and downlink power requirements. This asymmetry arises from the so-called shower curtain effect [9], [10], whereby the impact of a scattering layer depends on its position within the optical path. Since the ground station is located within the atmospheric scattering layer, the uplink is more severely degraded than the downlink, necessitating higher optical transmit power to compensate for atmospheric impairments. Consequently, scaling the optical power of ground station transmitters is a key requirement for achieving high data-rate satellite uplinks. A typical structure used for uplink optical transmission is shown in Fig. 1, where a standard optical transmitter (TX) prepares the signal and feeds it into a high-power optical amplifier (HPOA), which is required to achieve the high optical power needed for the application. An optical fiber (OF), e.g., an output pigtail or a short optical patch cord, delivers the signal to the optical ground station (OGS), which is used for beam preparation and pointing. In this context, external cavity lasers followed by fiber based HPOA represent a natural choice for OGS transmitters, owing to their capability to deliver high average power while maintaining excellent beam quality. Recently, several HPOAs have been demonstrated, including in-band core-pumped Er-doped fibers [11], cladding-pumped Er-doped fibers [12], and cladding-pumped ErYb co-doped fibers [13]. For example, in this paper we will consider as a typical example an HPOA made of an Er-doped fiber with large-core area of length 30m, with additional 3m of patch cords, with power up to 100 W. All these approaches exhibit physical and practical constraints or limitations, making custom designs necessary depending on the specific application [14]. Among the main challenges, fiber nonlinearities invariably arise when a high-power signal propagates through optical fibers—either within the doped fiber inside the amplifier or along the output pigtail or any additional patch cords. Its mitigation is essential to increase the launch power, thereby enabling higher throughput or longer transmission distances [15], [16]. On one hand, the nonlinearity can be mitigated by carefully designing the HPOA. For instance, erbium-doped fiber amplifiers (EDFAs) typically require relatively longer doped fiber compared to erbium-ytterbium codoped amplifiers (EYDFAs), making the latter a better options to counteract nonlinear effects. However, very high power EYDFAs suffer from higher-order mode power transfer leading to pointing stability fluctuation as well as long term power degradation due to photodarkening [14].

S. Civelli is with the Cnr-Istituto di Elettronica e di Ingegneria dell'Informazione e delle Telecomunicazioni (CNR-IEIIT), Pisa, Italy. S. Civelli, M. Secondini and E. Forestieri are with the Telecommunications, Computer Engineering, and Photonics (TeCIP) Institute, Scuola Superiore Sant'Anna, Pisa, Italy. M. Secondini, E. Forestieri and L. Potì with the National Laboratory of Photonic Networks, CNIT, Pisa, Italy. L. Potì is with the Universitas Mercatorum, Rome, Italy. Email: stella.civelli@cnr.it.

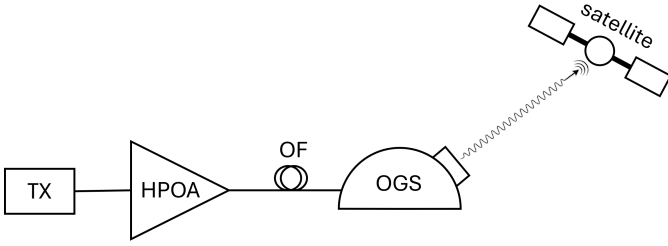


Figure 1. Ground-to-satellite optical link

Recently, an Er-based HPOA with power up to 50dBm was proposed, specifically designed to mitigate nonlinear effects; the proposed HPOA combines an EDFA to increase the power up to 27dBm and a large-mode-area EDFA to further amplify the signal (short fiber with low nonlinear Kerr parameter) [17]. However, the large-mode-area approach lacks commercially available and reliable components, and maintaining single-mode operation can be challenging. On the other hand, fiber nonlinearity can be mitigated by properly designing the signal and/or using digital signal processing (DSP). For example, the Kerr nonlinearity occurring in a short single-mode fiber (SMF) pigtail following an HPOA has been studied in [16], where a compensation method for direct detection systems was proposed. Furthermore, coherent communications have become a reality for space communications, enabling more advanced DSP and higher throughput [2], [18]. In this paper, we propose mitigation and compensation techniques for coherent optical satellite communication uplinks, introducing low-complexity DSP methods that enable higher launch power and, consequently, longer transmission distances or higher data rates. Here we extend the work in [19] providing a detailed model of the channel, a theoretical analysis of the impact of Kerr nonlinearity, and a comprehensive numerical analysis of the performance under different compensation techniques and scenarios.

The paper is organized as follows. Section II presents a comprehensive system model and introduces a simplified model that accurately captures the system behavior. Section III proposes two DSP techniques for the compensation of nonlinearity: probabilistic constellation shaping and nonlinear phase compensation (NLPC). Both Sections II and III provide a comparison with long-haul fiber systems, whose nonlinear effects have been thoroughly investigated over the past decades. Section IV presents the system setup and a detailed numerical analysis of the system and the proposed DSP techniques under different conditions. Finally, Section V draws the conclusions.

II. SYSTEM MODEL

We consider a coherent ground-to-satellite optical link, sketched in Fig. 1. Fig. 2 illustrates the equivalent complex baseband representation adopted throughout this work. The system comprises a ground-based transmitter, a short high-power optical fiber stage including amplification, an FSO link toward the satellite, and a coherent receiver. In the following, each subsystem is described in detail.

A. Transmitter

At the transmitter (TX), information bits are mapped by DSP onto a dual-polarization (DP) M -ary quadrature amplitude modulation (QAM) signal with baud rate R . The resulting complex baseband signal can be written as

$$\mathbf{x}(t) = \sum_k \mathbf{a}_k p(t - kT) \quad (1)$$

where $\mathbf{a}_k = [a_{k,x}, a_{k,y}]^T$ contains the couple of complex QAM symbols transmitted on the two orthogonal polarizations, $p(t)$ is the pulse shape, and $T = 1/R$ the symbol interval. Optional digital pre-distortion may be applied at this stage.

Each polarization component is decomposed into its in-phase and quadrature parts. Consequently, the DP signal is represented by four real-valued electrical waveforms (I/Q components for the two polarizations), which are converted into analog form by four digital-to-analog converters (DACs).

The resulting analog signals are applied to a dual-polarization IQ modulator, which maps them onto the two orthogonal polarization states of a continuous-wave optical carrier generated by a narrow-linewidth laser source. Under the complex baseband representation adopted in this work, the combined effect of DACs, drivers, and modulator bandwidth limitations is captured by $H_{TX}(f)$.

The resulting optical signal is subsequently amplified by an HPOA and delivered to the OGS output through a short fiber section (patch cord or pigtail).

B. Optical Fiber Channel

The optical signal propagates through two short fiber sections: the active fiber inside the HPOA and the passive delivery fiber (patch cord). Although their total length is typically below 100 m, the launched optical power may exceed 35–40 dBm, making nonlinear effects significant.

Propagation of the dual-polarization signal in both sections is described by the Manakov equation¹ for the complex envelope $\mathbf{u}(z, t) = [u_x(z, t), u_y(z, t)]^T$, normalized such that $E\{\|\mathbf{u}(z, t)\|^2\} = 1$

$$\frac{\partial \mathbf{u}}{\partial z} = j \frac{\beta_2}{2} \frac{\partial^2 \mathbf{u}}{\partial t^2} - j \gamma P g(z) \|\mathbf{u}\|^2 \mathbf{u} + \mathbf{n}_{ASE} \quad (2)$$

where P is the output optical power (on both polarizations), γ is the Kerr nonlinear coefficient, β_2 is the group-velocity dispersion, $g(z)$ is the normalized longitudinal power profile ($g(L) = 1$, with L the total fiber length) accounting for both gain and loss, and $\mathbf{n}_{ASE}(z, t)$ is the amplified spontaneous emission (ASE) noise. Below, the dominant physical effects are discussed.

¹The small random birefringence unavoidably present in optical fibers gives rise to an additional polarization-dependent nonlinear term. In standard telecom fibers, the birefringence correlation length is typically much shorter than the propagation distance. As a result, the contribution of this term averages out along the link and is generally negligible at the system level. Its possible relevance in the scenario considered here is left for future investigation. Other nonlinear mechanism (e.g., Raman, Brillouin, ...) are not included in the model, since Kerr effect is expected to be the dominant impairment [16].

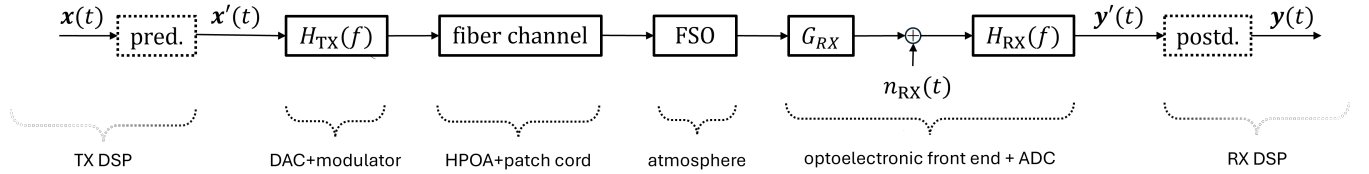


Figure 2. System model

1) *Amplification and Noise*: The HPOA is modeled as a distributed-gain active fiber generating ASE along the propagation coordinate z . The longitudinal power profile $g(z)$ and the power spectral density (PSD) of the ASE noise term $\mathbf{n}_{\text{ASE}}(z, t)$ are obtained from the standard coupled propagation and population equations governing doped-fiber amplifiers, evaluated under the assumption of a continuous-wave input signal and flat gain and ASE spectra over the signal bandwidth. Under these assumptions, the computed gain and noise profiles are treated as known quantities and incorporated into the normalized Manakov equation (2) to assess their impact on signal propagation. By contrast, the patch cord is a passive fiber, where $g(z)$ is determined only by fiber attenuation and no ASE noise is generated ($\mathbf{n}_{\text{ASE}}(z, t) = 0$).

As will be shown later, although gain and ASE are generated continuously along the HPOA, their detailed longitudinal distribution is irrelevant from a system-level perspective, since only the output quantities determine performance. To characterize them, we introduce two lumped parameters. The first is the amplifier gain $G^{\text{HPOA}} = P/P_{\text{IN}}$, defined as the ratio between output and input signal power. The second is the noise figure F_n^{HPOA} , which quantifies the degradation of the signal-to-noise ratio (SNR) introduced by the amplifier and therefore determines the PSD of the ASE noise accumulated at the signal output, $N_0^{\text{HPOA}} = G^{\text{HPOA}} F_n^{\text{HPOA}} h\nu/2$ (per polarization).

2) *Chromatic Dispersion*: The first term of the right-hand side of (2) is responsible for chromatic dispersion, which induces a temporal broadening of the propagating optical pulses. For a pulse of width T_0 , the amount of broadening increases with the ratio L/L_D , where

$$L_D \triangleq \frac{T_0^2}{|\beta_2|} \quad (3)$$

is the dispersion length [20, eq (3.1.5)]. We can readily verify that in the typical scenario considered in this work, $L \ll L_D$, indicating a negligible broadening of the propagating signal. For instance, for a 100 GBd signal in a standard SMF, assuming $\beta_2 = 21.7 \text{ ps}^2/\text{km}$ and $T_0 \approx T = 10 \text{ ps}$, $L_D \approx 4.6 \text{ km}$, whereas the total fiber length L is typically below 100 m.

3) *Kerr Nonlinearity*: In contrast, Kerr nonlinearity—the second term on the right-hand side of (2)—plays a central role due to the high optical power. When $L \ll L_D$, chromatic dispersion can be neglected and, in the absence of ASE noise, propagation is dominated by the Kerr nonlinear term. In this case, (2) can be solved in closed form as

$$\mathbf{u}(L, t) = \mathbf{u}(0, t) \exp(-j\bar{\phi} \|\mathbf{u}(0, t)\|^2) \quad (4)$$

with

$$\bar{\phi} = P \int_0^L \gamma g(z) dz \quad (5)$$

According to (4), the optical signal undergoes a phase rotation proportional to its instantaneous power, a phenomenon known as *self-phase modulation* (SPM). The strength of SPM depends on the dimensionless parameter $\bar{\phi}$ in (5), which represents the average accumulated nonlinear phase rotation (NLPR). For convenience, we rewrite it as $\bar{\phi} = P/P_{\text{NL}}$, where we have introduced the characteristic nonlinear power

$$P_{\text{NL}} = \left(\int_0^L \gamma g(z) dz \right)^{-1} \quad (6)$$

representing the power scale at which SPM becomes significant. For instance, the HPOA considered in Section IV-A has $P_{\text{NL}} \approx 42.7 \text{ dBm}$.

We distinguish three main effects associated with SPM.

a) *Nonlinear phase rotation (NLPR)*: Each received symbol undergoes a different power-dependent phase rotation. In the absence of chromatic dispersion, symbols do not spread nor interact through linear memory, and therefore the nonlinear distortion remains temporally uncorrelated. In principle, NLPR is a deterministic effect which can be exactly compensated by applying the inverse phase rotation at either the transmitter or the receiver, as discussed in Section III-B. In practice, however, compensation is fundamentally limited by the additional effects described below. Moreover, unlike long-haul dispersive links, the absence of temporal correlation in the NLPR prevents its mitigation through conventional carrier phase recovery algorithms that rely on temporal averaging [21].

b) *Spectral broadening*: SPM inherently implies spectral broadening, since the phase shift in (4) induces a time-varying frequency chirp that depends on the derivative of the signal intensity. In conventional systems operating on standard SMF fibers in the C band, spectral broadening is strongly suppressed by chromatic dispersion and is therefore typically negligible. By contrast, in the present scenario, where $L \ll L_D$, it may become significant. In this dispersionless regime, and under the assumption of independent and statistically equivalent polarizations with circularly symmetric complex Gaussian statistics, the evolution of the PSD can be derived analytically. Letting

$$R(z, \tau) \triangleq E\{u_x(z, t + \tau)u_x^*(z, t)\} = E\{u_y(z, t + \tau)u_y^*(z, t)\} \quad (7)$$

denote the autocorrelation function of each polarization component of the normalized envelope at distance z , one obtains (see Appendix)

$$R(L, \tau) = \frac{R(0, \tau)}{[1 + \bar{\phi}_{\text{NL}}^2(1/4 - |R(0, \tau)|^2)]^3} \quad (8)$$

The PSD follows from the Wiener–Khinchin theorem as

$$S(z, f) = \int_{-\infty}^{\infty} R(z, \tau) e^{-j2\pi f\tau} d\tau \quad (9)$$

Fig. 3(a) illustrates an example of spectral broadening occurring in an HPOA. The PSDs of the transmitted (left) and received (right) signal are shown. Numerical simulations based on the split-step Fourier method (SSFM), averaged over many realizations, are compared with the analytical prediction based on (8). The numerical results are obtained for probabilistically shaped 64-QAM signals with $R = 100\text{GBd}$ and root-raised cosine spectrum with roll-off 0.05 and $P = 43\text{dBm}$ (corresponding to $\bar{\phi} \approx 1.1$). Probabilistic shaping uses either i.i.d. symbols with a Maxwell–Boltzmann (MB) distribution or sphere shaping with block length 4 (sp. sh. $N = 4$). More details about probabilistic shaping and the simulation setup are provided later in Section IV-A. The numerical MB curves are superimposed with the analytical curves in (8), as the distribution is close to the Gaussian one assumed in the derivation of (8). By contrast, sp. sh. $N = 4$ exhibits less spectral broadening due to the strong correlation between the amplitudes of the four quadrature components of each DP symbol, which is not accounted for in the analytical model. The advantage resulting from this reduced spectral broadening will be discussed in greater detail later. In all cases, the received signals in Fig. 3(a) show a relevant spectral broadening.

Such bandwidth expansion, combined with the finite bandwidth of practical transmitters and receivers, may degrade system performance and fundamentally limit the compensation of NLPR. At the receiver, the transfer function $H_{\text{RX}}(f)$ filters out part of the spectrally broadened signal, preventing exact inversion of (4). Similarly, at the transmitter, accurate pre-compensation would require generating frequency components that may lie outside the available bandwidth defined by $H_{\text{TX}}(f)$.

c) Signal–noise interaction: During propagation inside the HPOA, ASE noise is continuously generated, as described by the distributed noise term in (2). In principle, this ASE component co-propagates with the signal and causes random intensity fluctuations that, through (4), are converted to random phase fluctuations (nonlinear phase noise).

In the considered scenario, however, the amount of ASE generated within the amplifier is typically negligible compared to other sources of noise in the system. As a consequence, the corresponding nonlinear signal–noise interaction is also negligible, and the overall SNR is essentially determined by the receiver noise.

On the other hand, receiver noise, although it does not physically interact with the signal inside the nonlinear fiber, may give rise to an indirect but analogous form of signal–noise interaction when attempting to invert (4) by DSP at

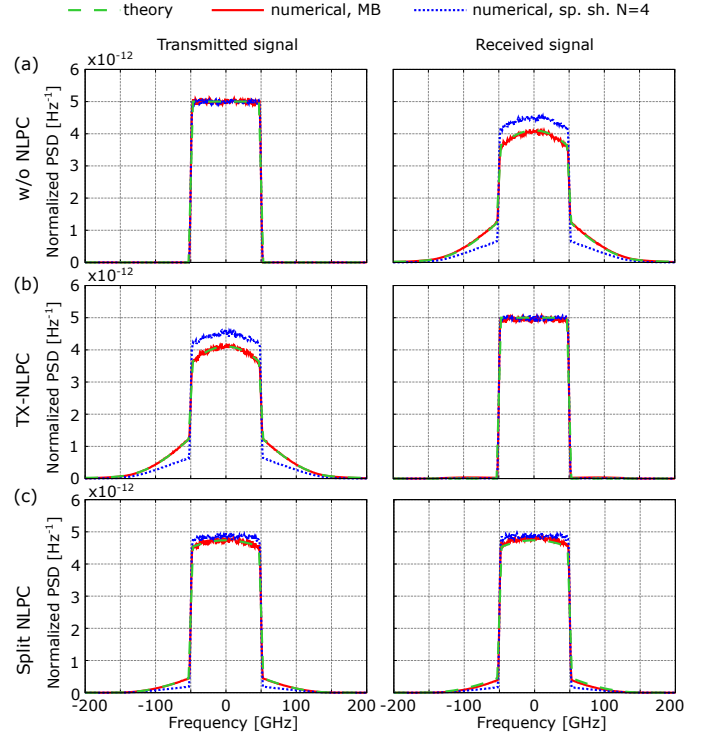


Figure 3. PSD of the normalized transmitted (left) and received (right) signals (100GBd, $\bar{\phi} \approx 1.1$) obtained analytically from (8) or with numerical simulations (MB and sph.sh. $N = 4$): (a) without NLPC; (b) with TX-side NLPC; and (c) with split NLPC. The details of the setup are reported in Section IV-A.

the receiver. This mechanism, which will be analyzed in the following, ultimately limits the practical mitigation of NLPR.

C. Free-Space Optical Channel

After leaving the OGS, the optical signal propagates through an FSO link toward the satellite.

All time-varying propagation effects—such as atmospheric turbulence, scattering, and molecular absorption—are treated in a static manner. The wireless channel is therefore simply modeled as a constant attenuation factor \mathcal{L} , representing the overall link loss between ground and satellite.

D. Receiver

At the receiver (RX), a preamplified coherent optoelectronic front-end is considered, comprising an optical pre-amplifier with gain G_{RX} and noise figure F_{RX} ; a polarization- and phase-diversity coherent receiver with balanced photodetectors; and four analog-to-digital converters (ADCs), one per each quadrature component of each polarization. The receiver is considered ideal, but for the finite electrical bandwidth of the photodetectors and ADCs, which is modeled by a low-pass transfer function $H_{\text{RX}}(f)$.

The digitized samples are finally processed by DSP, which includes optional NLPR compensation, matched filtering, and symbol-rate sampling. More details about DSP are provided in Section III and IV-A.

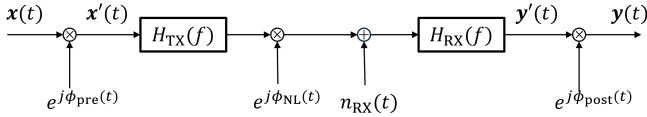


Figure 4. Simplified model

E. Simplified Model

Based on the above considerations, the baseband model in Fig. 2 can be simplified as in Fig. 4, where the fiber channel is simply modelled by the NLPR $\phi_{NL}(t) = -\bar{\phi}\|\mathbf{u}(0, t)\|^2$ in (4) (neglecting dispersion and signal–noise interaction), and the AWGN term $\mathbf{n}(t) = [n_x(t), n_y(t)]^T$ accounts for the contribution of all noise sources and for the effect of gains and losses, with an overall SNR (per symbol)

$$\text{SNR} = \frac{P}{R_s h\nu(\mathcal{L}F_{RX} + G_{HPOA}F_{HPOA})} \approx \frac{P}{R_s h\nu\mathcal{L}F_{RX}} \quad (10)$$

The approximation in (10) holds when $\mathcal{L} \gg G_{HPOA}$, i.e., in the practically relevant scenario of strong channel loss.

This simplified model captures the most relevant characteristics of the channel, namely, AWGN, bandwidth constraints, NLPR, and the associated spectral broadening. It will therefore be used in the following to design and optimize the system and to provide a theoretical interpretation of the results.

In particular, based on this model, we restrict transmitter pre-distortion and receiver post-compensation to simple phase rotations— $\phi_{pre}(t)$ and $\phi_{post}(t)$, respectively—as detailed in Section III-B.

On the other hand, simulation results will be obtained using the more accurate physical model described previously. Nevertheless, we will demonstrate that the simplified model reproduces them with good accuracy and can, in principle, replace the full physical model even for reliable performance estimation.

III. DIGITAL TECHNIQUES FOR NONLINEARITY COMPENSATION

In this section, we discuss and analyze DSP techniques for the mitigation of the HPOA nonlinearity. The proposed techniques are inherited from optical fiber communication and tailored to the HPOA scenario.

A. Probabilistic constellation shaping

Probabilistic constellation shaping has been known for several decades, and nowadays is commonly adopted in optical fiber coherent systems with the dual objective of improving system performance and enabling fine-tuning of the transmission rate. Probabilistic shaping is commonly implemented through the probabilistic amplitude shaping (PAS) architecture, in which a distribution matcher (DM) maps information bits onto shaped amplitudes, while the signs remain uniformly distributed and are used for forward error correction (FEC) [22]. The main component of PAS is the DM, which maps k information bits onto N shaped amplitudes (where N denotes the block length) drawn from the M -ary alphabet

$\{1, 3, \dots, 2M - 1\}$, achieving a DM rate $R_{DM} = k/N$. The N amplitudes are then combined with N signs (with uniform distribution), to form $N/4$ couples of complex QAM symbols modulating the signal in (1).² The accuracy of the DM depends on the specific implementation but typically improves when N increases [21], [23], [24]. In general, algorithmic DMs, such as constant-composition DM (CCDM), enumerative sphere shaping (ESS), and their variants, achieve good performance at the cost of non-negligible complexity for large N [23], [24]. By contrast hierarchical DMs based on look-up-tables (LUTs) have negligible complexity but reduced performance [25], [26]. When N is very small, the DM can be implemented efficiently with a single LUT, simply storing the 2^k best sequences of N amplitudes. In the linear regime, these correspond to the sequences with minimum energy. An example of encoding LUT containing minimum energy sequences is shown in Fig. 5 for $k = 5$, $N = 4$, and $M = 4$, ($R_{DM} = 1.25$ bits/amplitude, 64-QAM constellation). The k input bits determine the LUT address containing the output amplitude sequence. Correspondingly, the decoding LUT has M^N entries—one for each possible sequence of N amplitudes—each returning the associated k bits.³ Overall, the memory required for the encoding and decoding LUTs is $2^k N \log_2 M$ and $M^N k$ bits, respectively.

PAS provides two main advantages, discussed below: shaping gain and rate adaptability. Thanks to these features, PAS has also been proposed for free-space optical communications [18].

Rate adaptability refers to the ability to vary the information rate (IR) for a fixed FEC code rate c and constellation order, by solely adjusting the DM rate. Specifically, the information rate is given by $\text{IR} = R_{DM} - (1 - c)m$ in bits per 1D symbol, where $m = \log_2 M$ is the number of bits per amplitude [27]. This property is particularly attractive for satellite communications, where channel conditions can vary significantly, for instance due to cloud coverage. When using a LUT with block length N , the rate can be adapted by simply decreasing k —i.e., using only the first 2^k entries of the LUT—in steps of $1/N$, with finer granularity for larger N .

Shaping gain refers to the improved performance compared to uniform constellations. In the linear regime, PAS aims at reducing the mean energy per symbol for a fixed IR, and approaches Shannon capacity as N increases, providing up to 1.53dB gain over a uniform constellation by targeting the Maxwell–Boltzmann distribution, a sort of *discretized* Gaussian distribution.

PAS has also been investigated for mitigating nonlinearities in optical fiber communication, but with limited gains [21], [24], [28]. Here the mechanism relies on the correlations induced by the DM among the amplitudes within each block, which reduce the nonlinear interference generated during propagation. This effect is more pronounced for shorter block lengths N . As a result, the overall shaping gain is maximized

²Different mapping strategies are possible—e.g., mapping the DM amplitudes independently on each quadrature component of each polarization [21]—but are not considered in this work.

³Since not all M^N amplitude sequences are actually needed, a more efficient implementation of the decoding LUT may be devised.

index	LUT	energy
1	1111	4
2	1113	12
3	1131	12
4	1311	12
5	3111	12
6	1133	20
7	1313	20
...
32	5311	36

Input $k = 5$ bits → Output $N = 4$ amplitudes in $\{1,3,5,7\}$

rate 5/4, granularity by 1/4

Figure 5. LUT with $N = 4$ amplitudes from $\{1, 3, 5, 7\}$ and 32 entries ($k = 5$), corresponding to a 64QAM shaped constellation with rate 4.5bits/2D and sequences with minimum energy.

for a block length that balances linear and nonlinear effects and depends on the channel memory, i.e., on the accumulated dispersion. The optimal N is generally very long ($N > 100$) for multi-span fiber links (in C-band with SMF), and shorter ($N \sim 30$) for single-span links, but in any case too long for a single-LUT implementation. Moreover, the long memory of these fiber channels implies that carrier phase recovery algorithms that are commonly employed to address laser phase noise are also capable of mitigating the generated nonlinear interference, hiding the nonlinear shaping gain in most cases [21], [29].

The picture is quite different for satellite optical coherent up-links with HPOAs. While the behavior in the linear regime remains unchanged, the nonlinear regime differs due to the nearly dispersionless nature of the fiber channel, which makes nonlinearity an almost instantaneous (memoryless) effect, as discussed in Section II. This leads to two key consequences, which will be quantified and analyzed in Section IV-B: i) the optimal PAS block length N becomes much shorter, making a single-LUT implementation of the DM—such as the one depicted in Fig. 5—particularly attractive; ii) carrier phase recovery algorithms are ineffective in mitigating nonlinear interference, increasing the relevance of the nonlinear shaping gain provided by PAS.

B. Nonlinear phase compensation (NLPC)

Assuming the simplified model in Fig. 4, fiber propagation reduces to the phase rotation in (4), which can be inverted at the TX or RX DSP by applying the inverse rotation. We refer to this operation as *nonlinear phase compensation* (NLPC). In the absence of bandwidth limitations and noise, exact inversion could be equivalently performed at the TX or RX. In practice, however, bandwidth limitations and noise prevent exact inversion, as discussed in Section II.

To mitigate the effect of bandwidth limitations, it is advantageous to split the NLPC equally between TX and RX, minimizing the maximum spectral broadening experienced by the signal at both locations. As an example, Fig. 3 shows the PSD of the transmitted (left) and received (right) signals with different NLPC configurations (top: without NLPC, medium: with RX-side NLPC, bottom: with NLPC split between TX and RX), demonstrating that spectral broadening is minimized when NLPC is evenly divided between TX and RX.

On the other hand, noise is injected between the HPOA and the RX, breaking the symmetry between TX and RX process-

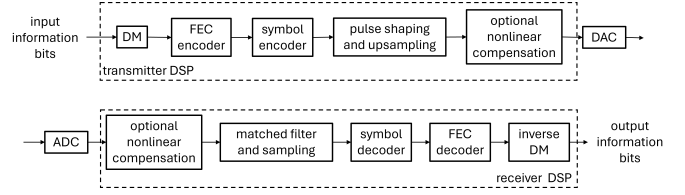


Figure 6. Transmitter and receiver DSP

ing and degrading only the effectiveness of RX-side NLPC. Furthermore, complexity and power consumption constraints are also asymmetric between satellite and ground terminals, generally favoring TX processing.

For these reasons, we consider a split NLPC between TX and RX, with splitting ratio κ

$$\mathbf{x}'[k] = \mathbf{x}[k] \exp(j\kappa\bar{\phi}\|\mathbf{x}[k]\|^2) \quad (11)$$

$$\mathbf{y}[k] = \mathbf{y}'[k] \exp(j(1-\kappa)\bar{\phi}\|\mathbf{y}'[k]\|^2) \quad (12)$$

where $\mathbf{x}[k]$, $\mathbf{x}'[k]$, $\mathbf{y}'[k]$, and $\mathbf{y}[k]$ denote the transmitted signal (before and after NLPC) and the received signal (before and after NLPC), respectively, as shown in Fig. 2 and 4, sampled at n samples per symbol. Based on the above discussion, the splitting ratio κ can be either optimized to maximize performance or set to $\kappa = 1$, corresponding to NLPC entirely performed at the TX. Both cases are analyzed in Section IV-B.

The complexity of NLPC, at the TX or RX side, measured as number of real multiplications (RM) per 2D symbols, is

$$C_{\text{NLC}} = 5.5n \text{ RM}/2\text{D} \quad (13)$$

assuming that each complex multiplication is implemented with 3 real multiplications [30].

IV. SYSTEM PERFORMANCE

A. System setup

System performance is evaluated through numerical simulations. A detailed system model is provided in Section II, while the transmitter and receiver DSP chains—operating with n samples/symbol—are shown in Fig. 6 and described below.

The TX-DSP, located at the ground station, maps information bits on symbols \mathbf{a}_k in (1) drawn from a DP M -QAM constellation with uniform distribution or probabilistically shaped distribution. In the latter case, the system uses the PAS approach, which combines DM and FEC in reverse concatenation order (the latter not included in our simulations) [22]. Unless otherwise stated, the pulse shape $p(t)$ in (1) has a root-raised cosine spectrum with roll-off 0.05, and the symbol rate is $R = 100$ GBd. An optional NLPC stage, defined in (11) and implemented with oversampling factor n , may be applied to (1) to obtain the signal $\mathbf{x}'(t)$.

Unless otherwise specified, the HPOA consists of an EDFA of length 30m with attenuation 0.2dB/km, nonlinear coefficient $3.6\text{W}^{-1}\text{km}^{-1}$, and dispersion $D = 17\text{ps/nm/km}$, followed by 3m of SMF fibers for pigtails and patch cords, resulting in an overall characteristic nonlinear power $P_{\text{NL}} \approx 42.7$ dBm. Fiber propagation according to (2) is evaluated numerically using the split-step Fourier method (SSFM) with a sufficiently large

number of steps, including dispersion, nonlinear Kerr effects, gain, and distributed noise due to ASE.

After the HPOA, the signal is launched into free space and received at the satellite station. Propagation through the FSO channel is simply modeled as a lumped attenuation \mathcal{L} . The noise figure of the RX-side EDFA is $F_{\text{RX}} = 4\text{dB}$. The limited bandwidth of both TX- and RX-side opto-electronics components (DAC, ADC, modulator and photoreceiver) is accounted for by ideal rectangular filters $H_{\text{TX}}(f) = H_{\text{RX}}(f)$ with lowpass bandwidth $B = 55\text{GHz}$. At the RX-DSP, an optional NLPC—defined in (12) and implemented with oversampling factor n as at the TX-side—can be applied, followed by matched filter and sampling at symbol time $1/R$. The resulting samples—a noisy version of the transmitted symbols—are compared with the transmitted symbols to evaluate the generalized mutual information (GMI), which quantifies the achievable information rate with ideal FEC and bit-wise decoding [31], [32]. In our simulations, the inverse DM and FEC decoding shown in Fig. 6 are not applied, since they are not required to compute the GMI. The TX and LO lasers are assumed ideal (zero linewidth), as the phase noise of typical telecom lasers at these baud rates can be effectively compensated by standard carrier phase recovery algorithms without performance penalty [33]. For a given launch power P , the performance is measured in terms of *acceptable link loss*, which is the maximum loss \mathcal{L} for which a desired GMI can be achieved. Our metric is analogous to the power budget—typically defined as the maximum allowable loss for a desired pre-FEC bit error rate (BER)—but replaces the pre-FEC BER threshold with a target GMI.⁴ In our setup, unless otherwise stated, we consider two cases: (i) target GMI = 3bits/2D on the shaped 64QAM constellation with shaping rate 4.5bits/2D or with uniform (U)-16QAM or 64QAM; and (ii) target GMI = 5bit/2D on the 256QAM constellation with shaping rate 6.5bits/2D or U-64QAM; the shaping rate has been optimized offline. Clearly, the acceptable link loss depends on the launched power P . It increases linearly with P until fiber nonlinearity remains negligible ($P \ll P_{\text{NL}}$), then reaches a peak at the optimal power and decreases afterwards due to the NLPR and spectral broadening induced by the nonlinearity. Accordingly, we define the *maximum acceptable link loss* as the peak value achieved at this optimal launch power.

B. System performance and gains

First, we analyze system performance for different modulation formats with uniform or shaped distributions. Fig. 7 shows the acceptable link loss versus launch power P for a target GMI = 3 bits/2D without NLPC, comparing U-16QAM, U-64QAM, i.i.d. symbols with MB distribution (an ideal benchmark distribution that is nearly optimal in the linear regime), and SpSh with very short ($N = 4$) and very long ($N = 256$) block lengths [24]. In all cases, PAS is

⁴Achieving the target GMI ensures that, with an ideal FEC, the system can operate at the corresponding bit rate (equal to the symbol rate multiplied by twice the GMI in bits per 2D symbol) with arbitrarily low error probability. For a specific realistic FEC, the target GMI can be replaced by the normalized GMI threshold evaluated for that FEC scheme [34].

implemented using 4D serial mapping: the N amplitudes from the same DM instance are mapped in serial to the quadratures and polarizations components of the symbols; overall $N/4$ 4D-symbols are generated from each DM instance, meaning that a DM with block length $N = 4$ generates a single 4D-symbol [21], [35]. The figure shows that (i) in the linear regime, ideal MB shaping achieves the best performance, closely approached by SpSh with $N = 256$; (ii) performance drops in the nonlinear regime due to HPOA-induced nonlinearity; and (iii) in the nonlinear regime, ideal MB shaping performs worse than uniform constellations, while SpSh with a very short block length provides the best performance despite its large rate loss in the linear regime. This behavior arises from a trade-off between linear shaping gain and robustness to nonlinear effects for the different formats. For a given average symbol energy, the linear shaping gain increases with the constellation entropy, reaching its maximum with MB shaping, whereas nonlinear effects grow with the energy variations among the constellation symbols—being absent in a 4D constant-energy constellation, lower for uniform constellations, and largest for MB. SpSh with $N = 256$ closely approximates MB shaping, while SpSh with $N = 4$ provides the best trade-off between linear gain and nonlinear robustness. The advantage of SpSh with $N = 4$ is also evident in Figs. 3(a-c), which show its reduced spectral broadening compared to MB shaping.

A deeper analysis of the behavior of different shaping strategies is reported in Fig. 8, which shows the maximum acceptable link loss (at optimal power, taken at 1dB steps) for different DM block lengths N for target GMI = 3 and without NLPC. The figure compares the performance of ideal i.i.d. symbols with MB distribution with that of SpSh, shell mapping [21], constant composition distribution matcher (CCDM) [23], and one example of hierarchical DM (HiDM) [25], [26].⁵ The figure shows that all techniques converge to the MB performance for long block lengths, with SpSh outperforming SM, which in turn outperforms CCDM. This behavior, also observed in conventional fiber systems, is due to the rate loss of the considered DMs, largest for CCDM and smallest for SpSh. By contrast, in this scenario, the optimal block length for SpSh and SM is much shorter ($N = 4$) than in conventional fiber systems [21], [36], [37], highlighting the importance of correlations between the four quadratures of a single 4D symbol rather than among adjacent symbols. Conversely, CCDM achieves its best performance with very long block lengths, due to the high rate loss incurred at short block lengths. The optimal SpSh with $N = 4$ can be implemented with a LUT with 32 entries, sketched in Fig. 5, containing the sequences of $N = 4$ amplitudes with lowest energy. Finally, HiDM (also implemented with LUTs) provides a good nonlinear performance, obtained with a longer block length $N = 64$, which may provide advantages in terms of rate granularity (by steps of $1/N$) and linear performance. Further optimization of HiDM may provide larger gains. In the following, unless otherwise stated, we consider as a

⁵The HiDM structure is made of 3 layers, with output amplitudes [4, 4, 4], input bits [1, 13, 12] and alphabet size [4, 64, 64] and has been optimized to have minimum rate loss under reasonable constraints and block length.

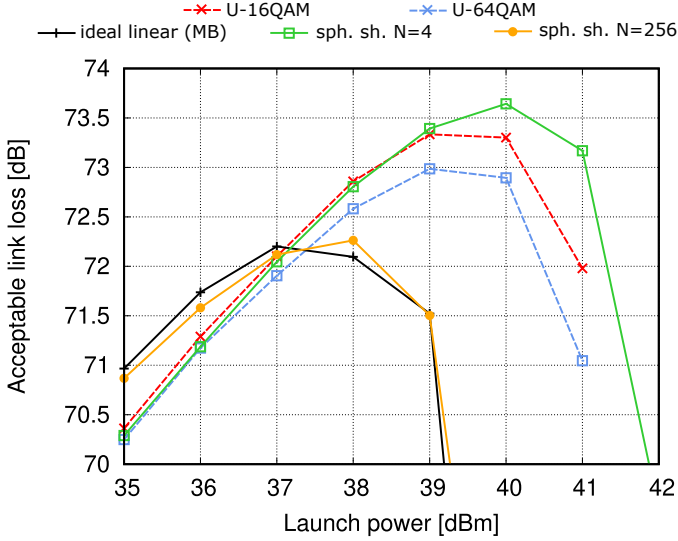


Figure 7. Acceptable link loss versus launch power for different DM techniques (GMI= 3, NLPC not applied)

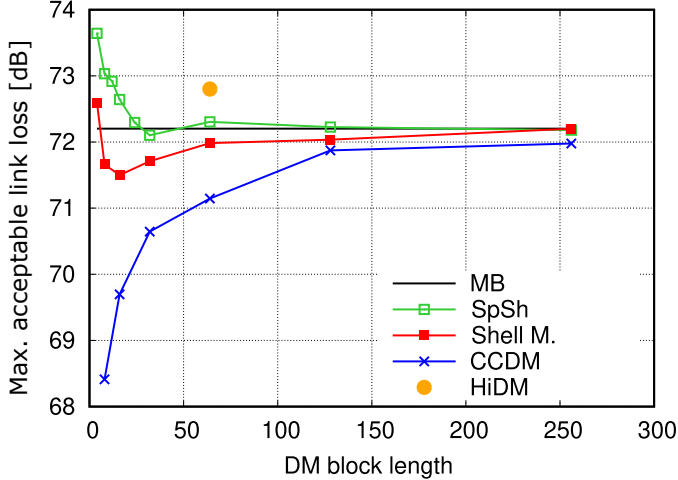


Figure 8. Maximum acceptable link loss versus DM block length for different DM techniques (GMI= 3, NLPC not applied).

modulation format sphere shaping with block length $N = 4$ (labeled as NL shaping).

Next, we show the performance with NLPC, optimizing the splitting ratio κ between TX and RX and the impact of DSP oversampling n . Fig. 9 reports the optimal performance, versus the splitting ratio κ , for $n = 8$. The performance is shown for GMI= 5 with solid lines and GMI= 3 with dashed lines (the same legend will be used in the following figures). For a discussion on the two GMI cases, the reader can refer to Fig. 11. Fig. 9 compares the results without NLPC (labeled NL shap.), with NLPC and 110GHz bandwidth limitations (labeled NL.shap.+split NLPC), with those with NLPC and ideal unlimited bandwidth B (labeled NL. shap. + split NLPC, unlimited bandwidth). Note, however, that the DSP bandwidth is limited by the number of samples n . NLPC is fully performed at the TX-side when $\kappa = 1$ (we indicate this as TX-NLPC in the following), while $\kappa = 0$ indicates that NLPC is performed at the RX-side. The latter case provides

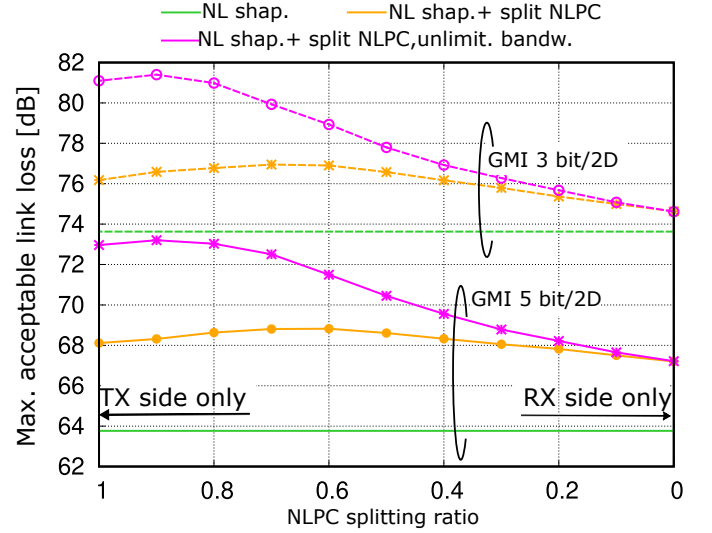


Figure 9. Maximum acceptable link loss versus NLPC splitting ratio κ , with $n = 8$.

the worst performance, approximately 1dB less than TX-side only, since NLPC is affected by RX-side noise; this is supported by the fact that also the curves with unlimited bandwidth drop. A good performance is obtained with TX-side only NLPC, with a gain of approximately 4dB and 2dB for GMI = 5 and GMI = 3, respectively. TX-NLPC has the additional advantage of applying this DSP only at the TX, making the RX at the satellite station simpler. Note that NLPC with unlimited bandwidth limitations does not provide the best performance for $\kappa = 1$, because it is limited by the oversampling factor $n = 8$. The optimal performance is obtained when $\kappa \approx 0.6$, with approximately 1dB gain w.r.t TX-NLPC, indicating a reasonable trade-off between bandwidth limitations (the spectral broadening is exactly split for $\kappa = 0.5$) and RX-side noise affecting NLPC (reduced for $\kappa > 0.5$). Figure 10 compares the optimal performance with TX-NLPC i.e., applying NLPC at the transmitter ($\kappa = 1$), NLPC with optimal splitting ($\kappa = 0.6$, denoted split NLPC), and TX-NLPC without bandwidth limitations, as a function of the oversampling factor n (bottom) and complexity (top), evaluated from Eq.(13). The figure shows that the performance of both TX and split NLPC saturates with $n = 2$ samples/symbol, when the 110GHz bandwidth limitation is included. The complexity of each NLPC is small and equals 11 RM/2D for $n = 2$. As expected, when the DAC and ADC bandwidth limitation is not included, the performance improves with larger n .

Next, Fig. 11 shows the performance versus power of the different considered techniques: (i) U-QAM constellations, (ii) constellation shaping with PAS optimized for the nonlinear regime using $N = 4$ and implemented with LUT (NL-shaping), (iii) NL shaping with TX-side NLPC, and (iv) NL shaping with NLPC split between TX and RX with $\kappa = 0.6$, all under 110GHz bandwidth limitations and with $n = 2$. As expected, the acceptable link loss with GMI= 3 is much higher—approximately 6dB in the linear regime and 10dB in the nonlinear regime (NL. shap.)—since a larger amount noise

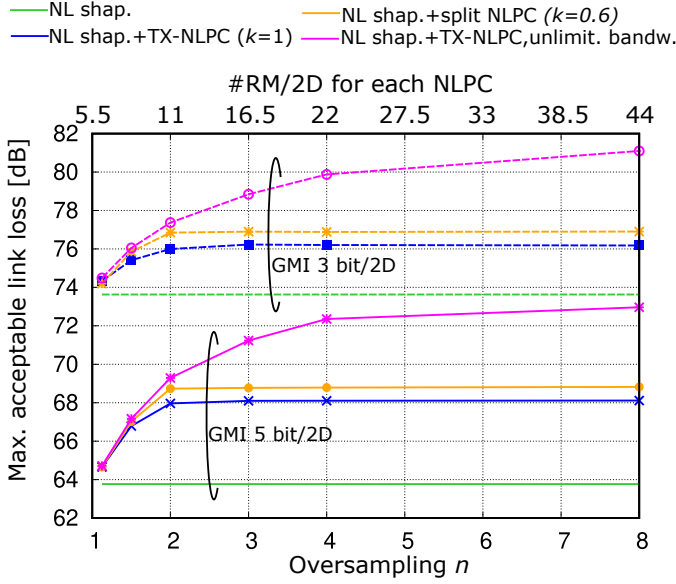


Figure 10. Maximum acceptable link loss versus DSP oversampling factor n (bottom) and DSP complexity (top) launch power for different DSP techniques, for GMI= 5 (solid) and GMI= 3 (dashed).

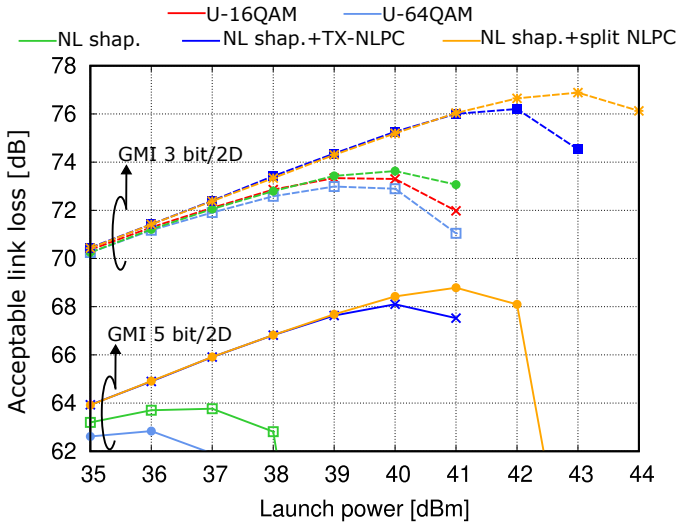


Figure 11. Acceptable link loss versus launch power for different DSP techniques, for GMI= 5 (solid) and GMI= 3 (dashed), with $n = 2$.

is supported. The figure shows that NL-shaping provides a small gain on top of uniform constellation, up to 1dB for GMI= 5, and provides approximately the same performance of uniform constellations in the linear regime (the conventional linear shaping gain disappears due to the large rate loss). Next, TX-side NLPC and split NLPC provides a larger gain, up to ≈ 4 dB and ≈ 5 dB, respectively, for GMI= 5.

Given a system with DAC and ADC bandwidth B , the symbol rate R should be optimized to obtain the best performance: either the largest acceptable link loss for a fixed bit rate, or the highest bit rate for a fixed acceptable link loss. Indeed, when $R \ll B$ the data rate is limited by the small symbol rate R , while in the other cases $R \approx B$ and $R \gg B$ part of information is cut by the ADC and DAC bandwidth limitations, and cannot be recovered even if NLPC is used. We

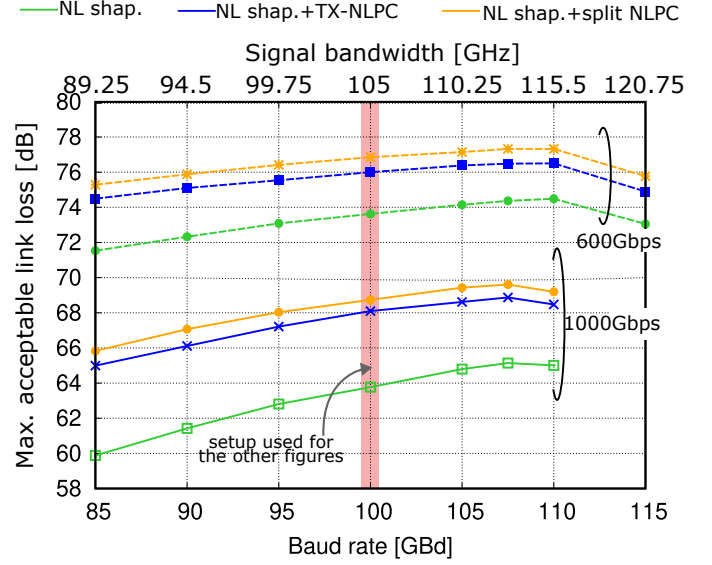


Figure 12. Maximum acceptable link loss versus Baud rate for different DSP techniques with $n = 2$. The GMI changes to have an overall net rate of 1000Gbps (solid) and 600Gbps (dashed). The top axis reports the signal bandwidth.

evaluate the optimal Baud rate and target GMI to achieve a target data rate $2RGMI$ in bit/s (the 2 stands for polarizations), under DAC and ADC bandwidth of $B = 110$ GHz. We consider the target rates (i) 600Gbit/s and (ii) 1000Gbit/s, corresponding to the cases GMI = 3 and GMI = 5 with $R = 100$ GBd considered above. The acceptable link loss is the maximum value obtained at the optimal power (sweeping the power by 1dB as in Fig. 11), as in Fig. 10. All curves are obtained with $n = 2$, changing R and selecting the target GMI as $GMI = (\text{target rate})/(2R)$. The signal bandwidth is $1.05 \cdot R_s$ considering the roll-off and is as large as the DAC/ADC bandwidth (110GHz) for approximately 105GBd (shown with the vertical dotted line). The figure shows that the largest link loss is obtained increasing the symbol rate R above 105GBd: in this case some information is cut but the required GMI is smaller, making the overall acceptable loss larger, for the same bit rate.

Finally, we compare the performance obtained with exactly zero dispersion—i.e., using the simplified model in Fig. 4—with that using different setups for the high power signal propagation where the nonlinearity originates:

- 1) the setup considered in this paper, i.e., one HPOA of length 33m with $\gamma = 3.6W^{-1}km^{-1}$ and $P_{NL} = 42.68$ dBm;
- 2) the setup considered in [16], with 3m of SMF ($\gamma = 1.27W^{-1}km^{-1}$) with $P_{NL} = 54.20$ dBm (this setup neglects the nonlinearity inside the amplifier but accounts only for that in the patchcord);
- 3) 43m of SMF ($\gamma = 1.27W^{-1}km^{-1}$) with $P_{NL} = 42.68$ dBm, for comparison among the first two cases (SMF propagation with the same γL_{eff} of 1);
- 4) the two stage-amplifier specifically designed in [17] to reduce nonlinearity—this setup is implemented in our simulation as a 6.2m doped fiber with $\gamma =$

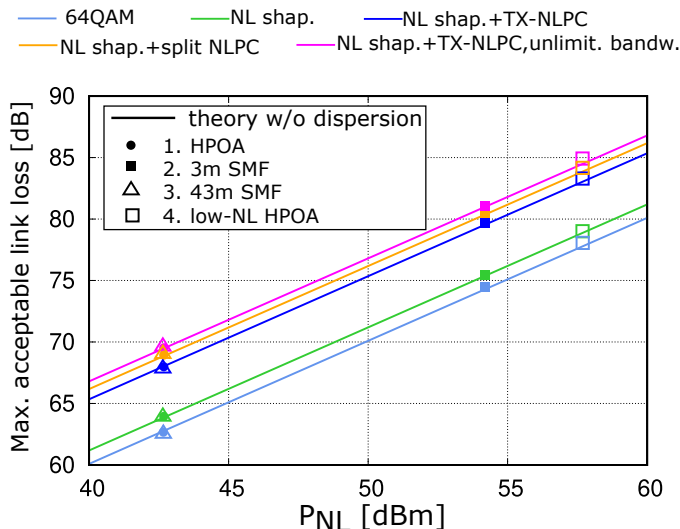


Figure 13. Maximum acceptable link loss as a function of the HPOA characteristic nonlinear power P_{NL} , for different HPOA configurations and NLPC techniques ($n = 2$). Target GMI = 5bits/2D.

$0.5\text{W}^{-1}\text{km}^{-1}$ which amplifies the signal from 27dBm to the desired power (for the sake of simplicity we neglect the first EDFA which has negligible nonlinear effects).

Fig. 13 shows the maximum acceptable link loss versus the characteristic nonlinear power $P_{NL} = (L_{\text{eff}}\gamma)^{-1}$. As expected, the figure shows that in the simplified dispersionless scenario (shown with a solid line) the link loss increases linearly with P_{NL} . Indeed, nonlinearity depends only on P/P_{NL} and when P_{NL} increases, the peak power P also increases, allowing a larger link loss. Interestingly, the performance of the different HPOA scenario (shown with symbols) lays on the dispersionless line, confirming that these scenarios can be equivalently represented by the simplified model in Fig. 4. Overall, Fig. 13 demonstrates that the performance in HPOA scenarios (high power and negligible dispersion) can be characterized and predicted simply using by P_{NL} , also when applying different DSP techniques, and that the simplified model in Fig. 4 can be used for design and testing of the more complex system in Fig. 2.

V. CONCLUSION

This work has presented a systematic analysis of coherent optical satellite uplink systems employing high-power optical amplifiers (HPOAs). To the best of our knowledge, this represents the first comprehensive investigation of nonlinear effects arising in the HPOA stage within this emerging application domain. In contrast to long-haul fiber links, dispersion in the considered scenario is negligible, and nonlinear distortions are essentially instantaneous, manifesting predominantly as self-phase modulation and spectral broadening. This fundamentally alters the interplay between nonlinearity, noise, and bandwidth limitations, leading to a distinct operating regime compared to conventional fiber systems.

In the ideal case of unlimited bandwidth, the instantaneous nature of the nonlinear distortion enables, in principle, perfect and low-complexity nonlinear compensation. However, in

practical systems subject to bandwidth constraints, nonlinear spectral broadening interacts with filtering and noise, making compensation more challenging. To address these limitations, digital signal processing techniques inherited from optical fiber communications have been adapted and optimized for the satellite uplink context.

First, probabilistic shaping has been investigated as a means to provide nonlinear gain, reduce spectral broadening, and enable rate granularity for adaptation to varying channel conditions. Different shaping implementations have been analyzed, showing that a simple look-up table (LUT)-based scheme, with negligible complexity, achieves the largest performance improvement, providing up to 1 dB of gain.

In addition, a low-complexity nonlinear phase compensation (NLPC) technique has been proposed, requiring only $5.5n$ multiplications per 2D symbol, where n denotes the number of samples per symbol. The NLPC can be implemented at the TX, at the RX, or split between the two. The analysis shows that optimal performance is achieved when the compensation is distributed between transmitter and receiver, with a splitting ratio of $\kappa = 0.6$, closer to the transmitter side to reduce the interaction with noise. Furthermore, it is shown that $n = 2$ samples per symbol are sufficient to achieve the best performance, confirming the feasibility of a low-complexity implementation.

Overall, the combination of probabilistic shaping and split NLPC provides gains of up to 4 dB and 6 dB in terms of tolerable loss with respect to uniform constellations for 600 Gb/s and 1 Tb/s transmission, respectively. The study also investigates the optimal baud rate vary under fixed bandwidth constraints, to achieve the same bit rate. Finally, it is demonstrated that the considered HPOA-based uplink scenario achieves performance consistent with a simplified dispersionless model, validating the adopted analytical framework and allowing easy performance prediction.

Future work will extend the present analysis to wavelength-division multiplexing (WDM) systems, where inter-channel nonlinear effects and spectral coexistence will introduce additional design trade-offs.

APPENDIX

We collect the two polarization components of the input field at times $t + \tau$ and t in the four-dimensional circularly symmetric complex Gaussian vector

$$\mathbf{z} = \begin{bmatrix} z_1 \\ z_2 \\ z_3 \\ z_4 \end{bmatrix} = \begin{bmatrix} u_x(0, t + \tau) \\ u_y(0, t + \tau) \\ u_x(0, t) \\ u_y(0, t) \end{bmatrix} \quad (14)$$

with probability distribution

$$p(\mathbf{z}) = \frac{1}{\pi^4 |\mathbf{C}|} \exp(-\mathbf{z}^H \mathbf{C}^{-1} \mathbf{z}) \quad (15)$$

where $\mathbf{C} = E\{\mathbf{z}\mathbf{z}^H\}$ is the covariance matrix and $(\cdot)^H$ denotes Hermitian conjugation. Assuming independent and statistically equivalent polarizations, \mathbf{C} has a simple block structure

$$\mathbf{C} = \mathbf{C}_2 \otimes \mathbf{I}_2, \quad \mathbf{C}_2 = \begin{bmatrix} R_0 & R_\tau \\ R_\tau^* & R_0 \end{bmatrix} \quad (16)$$

where \mathbf{I}_m is the $m \times m$ identity matrix,

$$R_0 \triangleq R(0,0), \quad R_\tau \triangleq R(0,\tau) \quad (17)$$

and \otimes denotes the Kronecker product. The determinant and inverse of \mathbf{C}_2 are

$$|\mathbf{C}_2| = R_0^2 - |R_\tau|^2, \quad \mathbf{C}_2^{-1} = \frac{1}{|\mathbf{C}_2|} \begin{bmatrix} R_0 & -R_\tau \\ -R_\tau^* & R_0 \end{bmatrix} \quad (18)$$

Letting

$$\mathbf{A} = \mathbf{A}_2 \otimes \mathbf{I}_2, \quad \mathbf{A}_2 = \text{diag}(1, -1) \quad (19)$$

the autocorrelation at distance L reads

$$\begin{aligned} R(L, t) &= E\{z_1 z_3^* \exp(-j\bar{\phi} \mathbf{z}^H \mathbf{A} \mathbf{z})\} \\ &= \frac{1}{\pi^4 |\mathbf{C}|} \int z_1 z_3^* \exp(-\mathbf{z}^\dagger \mathbf{D} \mathbf{z}) d\mathbf{z} \end{aligned} \quad (20)$$

where we have collected the terms at the exponent in a single quadratic form with matrix $\mathbf{D} = \mathbf{C}^{-1} + j\bar{\phi} \mathbf{A}$. Exploiting the block structure of \mathbf{C} and \mathbf{A} , we rewrite $\mathbf{D} = \mathbf{D}_2 \otimes \mathbf{I}_2$, with

$$\mathbf{D}_2 = \mathbf{C}_2^{-1} + j\bar{\phi} \mathbf{A}_2 = \frac{1}{|\mathbf{C}_2|} \begin{bmatrix} R_0 + j\bar{\phi} |\mathbf{C}_2| & -R_\tau \\ -R_\tau^* & R_0 - j\bar{\phi} |\mathbf{C}_2| \end{bmatrix} \quad (21)$$

A direct computation gives

$$|\mathbf{D}_2| = \frac{1 + \bar{\phi}^2 |\mathbf{C}_2|}{|\mathbf{C}_2|} \quad (22)$$

$$\mathbf{D}_2^{-1} = \frac{1}{1 + \bar{\phi}^2 |\mathbf{C}_2|} \begin{bmatrix} R_0 - j\bar{\phi} |\mathbf{C}_2| & R_\tau \\ R_\tau^* & R_0 + j\bar{\phi} |\mathbf{C}_2| \end{bmatrix} \quad (23)$$

Multiplying and dividing (20) by $|\mathbf{D}|$, we can interpret it as the expectation of $z_1 z_3^*$ under a Gaussian distribution with covariance matrix \mathbf{D}^{-1} , divided by the factor $|\mathbf{C}||\mathbf{D}|$. This expectation simply equals the corresponding term of the covariance matrix \mathbf{D}^{-1} , hence

$$R(L, t) = \frac{(\mathbf{D}^{-1})_{1,3}}{|\mathbf{C}||\mathbf{D}|} = \frac{(\mathbf{D}_2^{-1})_{1,2}}{|\mathbf{C}_2|^2 |\mathbf{D}_2|^2} \quad (24)$$

where the second equality follows from the properties of the Kronecker product. Replacing (18) and (22)–(23) in (24), we eventually obtain

$$R(L, \tau) = \frac{R_0}{[1 + \bar{\phi}^2 (R_0^2 - |R_\tau|^2)]^3} \quad (25)$$

Finally, using (17) and noting that the normalization adopted in the Manakov equation (2) implies $R_0 = R(0,0) = 1/2$, we obtain the expression (8) reported in the main text.

The analysis can be extended to the M -mode version of (2)—the so called *generalized Manakov equation*, which applies for instance to the propagation in multi-mode fibers in the strong coupling regime [38]. Defining a $2M$ -dimensional Gaussian vector \mathbf{z} with covariance matrix $\mathbf{C} = \mathbf{C}_2 \otimes \mathbf{I}_M$ (M independent and statistical equivalent modes), and following a similar derivation (replacing \mathbf{I}_2 with \mathbf{I}_M everywhere), one obtains

$$R(L, \tau) = \frac{R(0, \tau)}{[1 + \bar{\phi}^2 ((1/M)^2 - |R(0, \tau)|^2)]^{M+1}} \quad (26)$$

For $M = 1$, the well-known result for the scalar nonlinear Schrödinger equation is recovered [39], [40, eq. (4.1.20)] .

ACKNOWLEDGMENT

This work was supported by the European Union - Next Generation EU under the Italian National Recovery and Resilience Plan (NRRP), Mission 4, Component 2, Investment 1.3, CUP J53C22003120001, CUP B53C22003970001, partnership on “Telecommunications of the Future” (PE00000001 - program “RESTART”).

REFERENCES

- [1] H. Kaushal and G. Kaddoum, “Optical communication in space: Challenges and mitigation techniques,” *IEEE communications surveys & tutorials*, vol. 19, no. 1, pp. 57–96, 2016.
- [2] R. Li, B. Lin, Y. Liu, M. Dong, and S. Zhao, “A survey on laser space network: terminals, links, and architectures,” *IEEE Access*, vol. 10, pp. 34815–34834, 2022.
- [3] R. Boddeda, D. R. Arrieta, S. Almonacil, J. Renaudier, and S. Bigo, “Achievable capacity of geostationary-ground optical links,” *Journal of Lightwave Technology*, vol. 41, no. 12, pp. 3717–3725, 2023.
- [4] R. Boddeda, D. R. Arrieta, S. Bigo, S. Rabeh, S. Almonacil, A. Ghazisaeidi, E. Dutisseuil, H. Mardoyan, and J. Renaudier, “Current state, prospects, and opportunities for reaching beyond 100 gbps per carrier using coherent optics in satellite communications,” in *ECOC 2024; 50th European Conference on Optical Communication*, pp. 406–409, VDE, 2024.
- [5] R. Barrios, S. Dimitrov, R. Mata-Calvo, and D. Giggenbach, “Link budget assessment for geo feeder links based on optical technology,” *International Journal of Satellite Communications and Networking*, vol. 39, no. 2, pp. 160–177, 2021.
- [6] D. Giggenbach and A. Shrestha, “Atmospheric absorption and scattering impact on optical satellite-ground links,” *International Journal of Satellite Communications and Networking*, vol. 40, no. 2, pp. 157–176, 2022.
- [7] N. K. Lyras, C. I. Kourogiorgas, and A. D. Panagopoulos, “Cloud free line of sight prediction modeling for low earth orbit optical satellite networks,” in *International Conference on Space Optics ICSO 2018*, vol. 11180, pp. 555–563, SPIE, 2019.
- [8] L. C. Roberts Jr, S. R. Meeker, J. Tesch, J. C. Shelton, J. E. Roberts, S. F. Fregoso, T. Troung, M. Peng, K. Matthews, H. Herzog, *et al.*, “Performance of the adaptive optics system for laser communications relay demonstration’s ground station 1,” *Applied Optics*, vol. 62, no. 23, pp. G26–G36, 2023.
- [9] I. Dror, A. Sandrov, and N. S. Kopeika, “Experimental investigation of the influence of the relative position of the scattering layer on image quality: the shower curtain effect,” *Applied optics*, vol. 37, no. 27, pp. 6495–6499, 1998.
- [10] D. Aviv, *Laser space communications*. Artech, 2006.
- [11] L. V. Kotov, V. Temyanko, M. M. Bubnov, D. S. Lipatov, A. S. Lobanov, A. Abramov, S. S. Aleshkina, A. N. Guryanov, and M. E. Likhachev, “High-energy single-frequency core-pumped Er-doped fiber amplifiers,” *Journal of Lightwave Technology*, vol. 41, no. 5, pp. 1526–1532, 2022.
- [12] L. V. Kotov, M. E. Likhachev, M. M. Bubnov, O. I. Medvedkov, M. V. Yashkov, A. N. Guryanov, S. Février, J. Lhermite, and E. Cormier, “Yb-free Er-doped all-fiber amplifier cladding-pumped at 976 nm with output power in excess of 100 W,” in *Fiber Lasers XI: Technology, Systems, and Applications*, vol. 8961, pp. 149–154, SPIE, 2014.
- [13] T. Matniyaz, F. Kong, M. T. Kalichevsky-Dong, and L. Dong, “302 W single-mode power from an Er/Yb fiber MOPA,” *Optics Letters*, vol. 45, no. 10, pp. 2910–2913, 2020.
- [14] J. W. Nicholson, A. Grimes, B. Zhu, C. Jin, V. S. Sudarshanam, A. Hariharan, and D. J. DiGiovanni, “High-power fiber lasers for free-space optical communication uplinks,” *IEEE Journal of Selected Topics in Quantum Electronics*, 2025.
- [15] V. Billault, S. Leveque, A. Maho, M. Welch, J. Bourderionnet, E. Lallier, M. Sotom, A. L. Kerneç, and A. Brignon, “Optical coherent combining of high-power optical amplifiers for free-space optical communications,” *Optics Letters*, vol. 48, no. 14, pp. 3649–3652, 2023.
- [16] E. Ciaramella and G. Cossu, “Nonlinear fiber effects in ultra-high power 10×10 gbit/s WDM-IM free-space systems for satellite links,” *Optics Express*, vol. 32, no. 5, pp. 7959–7968, 2024.
- [17] A. Grimes, B. Zhu, C. Jin, and J. W. Nicholson, “10 gbps transmission from a high power edfa for free space communications,” in *2024 IEEE Photonics Society Summer Topicals Meeting Series (SUM)*, pp. 1–4, IEEE, 2024.

- [18] F. P. Guiomar, M. A. Fernandes, J. L. Nascimento, V. Rodrigues, and P. P. Monteiro, "Coherent free-space optical communications: Opportunities and challenges," *Journal of Lightwave Technology*, vol. 40, no. 10, pp. 3173–3186, 2022.
- [19] S. Civelli, M. Secondini, and L. Potì, "Nonlinearity mitigation for coherent ground-to-satellite optical links," *arXiv preprint arXiv:2601.05655*, 2026.
- [20] G. P. Agrawal, *Nonlinear fiber optics*. Academic Press, 2001.
- [21] S. Civelli, E. Forestieri, and M. Secondini, "On the nonlinear shaping gain with probabilistic shaping and carrier phase recovery," *Journal of Lightwave Technology*, vol. 10, no. 41, pp. 3046–3056, 2022.
- [22] G. Böcherer, F. Steiner, and P. Schulte, "Bandwidth efficient and rate-matched low-density parity-check coded modulation," *IEEE Transactions on Communications*, vol. 63, no. 12, pp. 4651–4665, 2015.
- [23] P. Schulte and G. Böcherer, "Constant composition distribution matching," *IEEE Transactions on Information Theory*, vol. 62, no. 1, pp. 430–434, 2016.
- [24] Y. Gültekin, W. van Houtum, and F. Willems, "On constellation shaping for short block lengths," in *2018 Symposium on Information Theory and Signal Processing in the Benelux (SITB 2018)*, pp. 86–96, University of Twente, 2018.
- [25] T. Yoshida, M. Karlsson, and E. Agrell, "Hierarchical distribution matching for probabilistically shaped coded modulation," *Journal of Lightwave Technology*, vol. 37, no. 6, pp. 1579–1589, 2019.
- [26] S. Civelli and M. Secondini, "Hierarchical distribution matching for probabilistic amplitude shaping," *Entropy*, vol. 22, no. 9, p. 958, 2020.
- [27] F. Buchali, F. Steiner, G. Böcherer, L. Schmalen, P. Schulte, and W. Idler, "Rate adaptation and reach increase by probabilistically shaped 64-qam: An experimental demonstration," *Journal of Lightwave Technology*, vol. 34, no. 7, pp. 1599–1609, 2016.
- [28] T. Fehenberger, A. Alvarado, G. Böcherer, and N. Hanik, "On probabilistic shaping of quadrature amplitude modulation for the nonlinear fiber channel," *Journal of Lightwave Technology*, vol. 34, no. 21, pp. 5063–5073, 2016.
- [29] S. Civelli, E. Forestieri, and M. Secondini, "Sequence-selection-based constellation shaping for nonlinear channels," *Journal of Lightwave Technology*, vol. 42, no. 3, pp. 1031–1043, 2024.
- [30] A. Wenzler and E. Luder, "New structures for complex multipliers and their noise analysis," in *1995 IEEE International Symposium on Circuits and Systems (ISCAS)*, vol. 2, pp. 1432–1435, IEEE, 1995.
- [31] A. Alvarado, T. Fehenberger, B. Chen, and F. M. Willems, "Achievable information rates for fiber optics: Applications and computations," *Journal of Lightwave Technology*, vol. 36, no. 2, pp. 424–439, 2018.
- [32] T. Fehenberger, D. S. Millar, T. Koike-Akino, K. Kojima, and K. Parsons, "Multiset-partition distribution matching," *IEEE Transactions on Communications*, vol. 67, no. 3, pp. 1885–1893, 2018.
- [33] T. Pfau, S. Hoffmann, and R. Noé, "Hardware-efficient coherent digital receiver concept with feedforward carrier recovery for m -qam constellations," *Journal of Lightwave Technology*, vol. 27, no. 8, pp. 989–999, 2009.
- [34] J. Cho, L. Schmalen, and P. J. Winzer, "Normalized generalized mutual information as a forward error correction threshold for probabilistically shaped QAM," in *2017 European Conference on Optical Communication (ECOC)*, pp. 1–3, IEEE, 2017.
- [35] T. Fehenberger, D. S. Millar, T. Koike-Akino, K. Kojima, K. Parsons, and H. Griesser, "Analysis of nonlinear fiber interactions for finite-length constant-composition sequences," *Journal of Lightwave Technology*, vol. 38, no. 2, pp. 457–465, 2020.
- [36] T. Fehenberger, H. Griesser, and J.-P. Elbers, "Mitigating fiber nonlinearities by short-length probabilistic shaping," in *Optical Fiber Communication Conference*, pp. Th11–2, Optical Society of America, 2020.
- [37] K. Wu, G. Liga, M. Secondini, and A. Alvarado, "Accounting for temporal energy correlations in the enhanced gaussian noise model," in *2025 Optical Fiber Communications Conference and Exhibition (OFC)*, pp. 1–3, IEEE, 2025.
- [38] A. Mecozzi, C. Antonelli, and M. Shtaif, "Nonlinear propagation in multi-mode fibers in the strong coupling regime," *Optics express*, vol. 20, no. 11, pp. 11673–11678, 2012.
- [39] J. T. Manassah, "Self-phase modulation of incoherent light revisited," *Optics letters*, vol. 16, no. 21, pp. 1638–1640, 1991.
- [40] G. P. Agrawal, *Fiber-optic communication systems*. John Wiley & Sons, 2012.